Microchimica Acta (2022) 189: 166
https://doi.org/10.1007/s00604-022-05280-y

ORIGINAL PAPER

Sensitive photoelectrochemical detection of colitoxin DNA based on NCDs@CuO/ZnO heterostructured nanocomposites with efficient separation capacity of photo-induced carriers

Delun Zheng[1,2] · Jianying Yang[3] · Zengyao Zheng[3] · Mingxuan Peng[1] · Kwan-Ming Ng[1] · Yaowen Chen[1] · Linjia Huang[4] · Wenhua Gao[1]

Received: 8 December 2021 / Accepted: 11 March 2022 / Published online: 30 March 2022

Abstract

A metal–organic framework (MOF) of Cu-TPA (terephthalic acid) microsphere was prepared, followed by calcinating the MOF precursor of Cu-TPA/ZIF-8 mixture to obtain the CuO/ZnO. N-doped carbon dots (NCDs) were employed to combine the CuO/ZnO composite to form a tripartite heterostructured architecture of NCDs@CuO/ZnO, which led to a fierce enlargement of the photocurrent response. This was ascribed to the thinner-shell structure of the CuO microsphere and the fact that hollow ZnO particles could sharply promote the incidence intensity of visible light. The more porous defectiveness exposed on CuO/ZnO surface was in favor of rapidly infiltrating electrolyte ions. The p-n type CuO/ZnO composite with more contact interface could abridge the transfer distance of photo-induced electron (e^{-1})/hole (h^{+}) pairs and repress their recombination availably. NCDs not only could boost electron transfer rate on the electrode interface but also successfully sensitized the CuO/ZnO composite, which resulted in high conversion efficiency of photon-to-electron. The probe DNA (S1) was firmly assembled on the modified ITO electrode surface (S1/NCDs@CuO/ZnO) through an amidation reaction. Under optimal conditions, the prepared DNA biosensor displayed a wide linear range of $1.0\times10^{-6}\sim7.5\times10^{-1}$ nM and a low limit of detection (LOD) of 1.81×10^{-7} nM for colitoxin DNA (S2) measure, which exhibited a better photoelectrochemistry (PEC) analysis performance than that obtained by differential pulse voltammetry techniques. The relative standard deviation (RSD) of the sensing platform for target DNA detection of 5.0×10^{-2} nM was 6.3%. This proposed DNA biosensor also showed good selectivity, stability, and reproducibility, demonstrating that the well-designed and synthesized photoactive materials of NCDs@CuO/ZnO are promising candidates for PEC analysis.

Keywords Photoelectrochemical · NCDs@CuO/ZnO composite · Tripartite-heterostructure · DNA biosensor

Introduction

The photoelectrochemical (PEC) technique not only inherits the advantages of electrochemical methods such as simplicity, portability, and easiness to miniaturize but also possesses lower bias potentials and higher sensitivity than its electrochemical counterparts [1]. Recently, PEC fabricated biosensors have widely gained attention such as the simultaneous detection of multiple micro-RNAs biomarkers [2], the biomolecules of cells [3], DNA [4], antibiotics [5], and so forth [6]. To obtain high-performance PEC biosensors for DNA detection, the photoactive and electrocatalytic materials play an important role that can significantly influence the improvement of the analytical sensitivity [7 ~ 9]. Moreover, an effective immobilization of the single-stranded probe DNA (S1) on the modified interface is indispensability,

✉ Wenhua Gao
whgao@stu.edu.cn

1 Department of Chemistry and Laboratory for Preparation and Application of Ordered Structural Materials of Guangdong Province, Shantou University, Shantou, Guangdong 515063, People's Republic of China

2 Department of Natural Sciences, Shantou Polytechnic, Shantou, Guangdong 515078, People's Republic of China

3 Guangdong Shantou Supervision Testing Institute of Quality & Measuring, Shantou, Guangdong 515041, People's Republic of China

4 Institute of Chemical Engineering, Guangdong Academy of Sciences, Guangzhou, Guangdong 510665, People's Republic of China

which relates to various properties of the biosensor such as accuracy, stability, and lifetime. Therefore, the design and synthesis of the excellent photoactive material are still urgently needed, as well as a well-defined matrix interface for functional immobilization should be carefully thought.

So far, various photoactive materials such as TiO_2 [10], CuO [11, 12], ZnO [13], Bi_2S_3 [14], and CdS [15] have been employed for the construction of PEC sensor. Among them, CuO has received extensive concern owing to its narrow band gap (1.4 ~ 1.7 eV) [16] and good electron conductivity. ZnO has a wide band energy gap (*Eg*) and shows the photo-activity performance only in the UV light region [17]. Moreover, due to the fast recombination of photo-induced carriers, the photocatalytic efficiency of ZnO is restricted [18]. And the pure photoactive material's inherent defects such as rapid recombination of electron–hole pairs and poor capability for visible light absorption, limit their further application in PEC analysis [19]. Considerable efforts have been transformed for coupling varieties of photoactive materials with better-matched energy levels to form the heterostructure composite which can extend the visible spectral range and accelerate charge carrier separation, resulting in promoted photocurrent output [20, 21].

Being a porous material, metal–organic frameworks (MOFs) are constructed by transition metal ions and organic ligands. Due to the specific surface area, exposed active sites, and versatile structures, MOFs have been extensively applied in the area of supercapacitors [22], catalysis [23], sensing [24], etc. Recently, the MOF precursors are employed to fabricate functional materials because of their controllable properties. By treating the precursor template under specific conditions, MOFs can be adjusted to the tailored morphologies such as hollow cages, hierarchical structures, and heterojunction composite [25, 26]. MOF-derived products can be the main structure of the MOF precursor morphologies, as well as owe the merit of combing various components such as metal oxides and metal sulfide [27, 28]. Further, through controlling the pore size and crystalline structure, MOF-ramification can provide more photocatalytic and electrochemical active sites, which greatly promote the ion diffusion and the electron transport rate [29]. Hu et al. [30] prepared a hierarchically structured octahedral CuO by treating a Cu-MOF precursor (HKUST-1) at alkaline conditions, exhibiting an ultra-high capacity for the Li + storage. Zhang et al. [31] constructed a core/shell nanocomposites of Fe_3O_4@C/Cu(CuO) through calcining the mixture of Fe_3O_4 and HKUST-1, which showed an obvious photocatalytic activity for the degradation of methylene blue (MB). Our work [32] had reported a hierarchical hollow ZnCdS@MoS_2 heterostructure cage which derived from ZIF-8 polyhedral cages and obtained greatly amplifying photocurrents response because of the close contact heterojunction interface. Thus, MOF-derivatives can be used as the great potential of photoactive materials to fabricate PEC biosensors.

Carbon dots (CDs) are assembled by carbon atom aggregates or small graphene nanoplatelets [33]. The typical size of CDs is in the range of about ~ 10 nm and with a relatively narrow band gap. Compared to the semiconductor materials or other metal complexes, CDs are more environmentally friendly and can be used as an ideal optical material [34]. Based on its excellent properties of photo-stability, biocompatibility, and easily functionalized as interface matrix, CDs have been widely applied in photocatalysis [35], optical imaging [36], sensors [37], etc. But a disadvantage of the poor electron transfer capability of CDs still limits its practical applications in electrochemical analysis. To overcome this problem, heteroatoms doping with N or S were proposed, and the obtained doped-CD composite not only shows an improvement in electro-catalysis property but also can improve significantly the optical capability [38]. For instance, Shi et al. [35] prepared the N-doped CDs (NCDs) with different atom ratios of N/C and the maximum level of N atom doping showed an enhanced electron transfer rate. Our work [40] previously synthesized NCDs could successfully sensitize the photoactive material of TiO_2 and further improve the photo-to-electron conversion efficiency of NCDs/TiO_2 composite.

Inspired by this, a novel Cu-TPA microsphere and its composite of Cu-TPA/ZIF-8 were successively synthesized. Through calcination, the Cu-TPA/ZIF-8 precursor template had a compact connective hetero-constructed composite of CuO/ZnO. Afterward, NCDs were assembled onto CuO/ZnO surface and the formed NCDs@CuO/ZnO showed the greatest photocurrent response signal than the CuO or CuO/ZnO composite, which could be explained as following reasons: (i) the well-matched energy band gaps of CuO, ZnO, and NCDs (*Eg* = 1.78, 3.20, and 2.98 eV, respectively) made the tri-heterojunction interfaces to accelerate the separation/migration of e^{-1}/h^+ carriers; (ii) the thin-shell structure of CuO and hollow polyhedron of ZnO could improve the light-absorption capability; (iii) the close contact CuO/ZnO interface with p-n type heterostructured system could shorten the carrier transfer distance and facilitate photo-to-electron conversion; (iv) the heterogeneous CuO/ZnO composite could be sensitized effectively by the NCDs which led to an enhanced photocurrent output. It was notable that NCDs were also employed as a functional matrix material for immobilization of the single-stranded probe DNA (S1) through a gentle amidation reaction between carboxyl groups (-COOH) and amino groups (-NH_2). The obtained probe modified electrode of S1/NCDs@CuO/ZnO/ITO was finally applied to detect the colitoxin DNA (S2). The photoactive material of NCDs@CuO/ZnO could further expand its tremendous application such as the photocatalytic production of hydrogen or the pollutant degradation.

Experimental section

The reagents and apparatus (the other reagents and apparatus are shown in the Electronic Supporting Material (ESM))

Reagents

Copper nitrate trihydrate ($Cu(NO_3)_2{\cdot}3H_2O$, 99%), benzene-1,3,5-tricarboxylic acid (BTC, 99%), terephthalic acid (TPA), and phosphate buffer (PB, $Na_2HPO_4{\cdot}12H_2O$/KH_2PO_4) were purchased from Aladdin Chemical Reagent Co., Ltd. (Shanghai, China). Ethylenediaminetetraacetic acid (EDTA), ethyl-3-(3-dimethylaminopropyl) carbodiimide (EDC, 99%), N-hydrosulfosuccinimide (NHS, 99.8%), and Tris (hydroxymethyl) aminomethane (Tris) were obtained from Sinopharm Chemical Reagent Co., Ltd. (China). Ammonium citrate and ethylenediamine were obtained from Xilong Chemical Co. Ltd. (Shantou, China). The other reagents were of analytical grade and gained commercially. All aqueous solutions were prepared with the deionized water.

Apparatus

The electrochemical experiments were carried out on a CHI 650E electrochemical analyzer (Shanghai CH Instrument Company). The conventional three-electrode system was consisted of bare or modified indium tin oxide (ITO) as working electrode, Ag/AgCl/(3 M) as reference electrode, and Pt wire as auxiliary electrode. The irradiation light source was from a 300-W Xe lamp, and the light intensity was measured using a touch screen thorlabs (PM200, USA).

*Synthesis of Cu-TPA, Cu-TPA/ZIF-8, and NCD*s.

The Cu-TPA (TPA: terephthalic acid) was synthesized by a solvothermal method according to reported literature [41] with a modification. Firstly, 0.6 g $Cu(NO_3)_2{\bullet}3H_2O$ (2.48 mmol) with 0.3 g TPA (1.8 mmol) was dissolved in 10 mL deionized water; then, 10 mL N, N-dimethylformamide (DMF) and and 10 mL ethanol were added into the above solution. Subsequently, the mixture was stirred for 30 min and transferred into a Teflon-lined stainless steel reactor (50 mL) with a treatment of heating at 95 °C for 24 h. After cooling to room temperature, the products were carefully gathered through centrifugation (8000 rpm, 10 min), washed with water and ethanol, and dried at 60 °C for 6 h under vacuum. Finally, the blue Cu-TPA particles were obtained.

The Cu-TPA/ZIF-8 composite was prepared as follows: 0.11 g of as-prepared Cu-TPA and 0.09 g of $Zn(NO_3)_2{\bullet}6H_2O$ (0.3 mmol) were dissolved in 50 mL methanol and treated with sonication to form a well-dispersed solution. Then, 0.22 g of 2-methylimidazole (0.26 mmol) was added into the mixture under stirring and reacted for 6 h. After that, the gained products of Cu-TPA/ZIF-8 were washed by centrifugation (8000 rpm, 10 min) with water and ethanol, respectively. ZIF-8 was synthesized in the above experiment process without adding the Cu-TPA.

NCDs were prepared by the hydrothermal method [40]. Under stirring, 1.0 g of ammonium citrate and 5 mL of ethylenediamine were dispersed in 10 mL deionized water. The mixture was subsequently transferred to a 50 mL Teflon-lined stainless steel reactor and heated for 5 h at 200 °C. The obtained orange-red solution was centrifuged (10,000 rpm, 10 min) and concentrated supernatant was further dialyzed for 24 h with the membranes of 1000 cutoffs. After freeze-drying at the vacuum condition, the brown N-doped CD powder was gained.

Preparation of CuO/ZnO and CuO/ZIF-8 composite

The as-fabricated Cu-TPA/ZIF-8 MOF precursors were transferred into a muffle furnace and calcined at 400 °C for 1.5 h. When cooling down to room temperature naturally, the dark gray product of CuO/ZnO was obtained. The CuO and ZnO particles were prepared in the same experimental condition without adding ZIF-8 or Cu-TPA. CuO was mixed with ZIF-8 (1:1, m/m) to obtain the CuO/ZIF-8 composite.

Fabrication of the DNA biosensor

Before modification, the ITO electrode was severally washed with acetone, 1.0 M NaOH, and deionized water three times. Subsequently, 8 µL suspension solutions (1.3 mg mL^{-1}) of CuO/ZnO were drop-cast on the cleaned ITO electrode surface and dried naturally. Then, the CuO/ZnO modified ITO electrode (CuO/ZnO/ITO) was immersed into 1 mg mL^{-1} NCD solution for 6 h. After thorough coupling, the desired electrode was marked as NCDs@CuO/ZnO/ITO.

The NCDs@CuO/ZnO/ITO electrode was immersed into 0.5 mL PBS solution (50 mM) with 20 mM NHS (N-hydrosulfosuccinimide) and 8 mM EDC (ethyl-3-(3-dimethylaminopropyl) carbodiimide) for 15 min in order to reactivate the carboxylic groups. After rinsing the modified electrode with the TE buffer solution (10 µM Tris–HCl, 1.0 mM EDTA, pH 8.0), 10 µL 0.1 µM S1 was dropped onto as-prepared NCDs@CuO/ZnO/ITO electrode for incubating 3 h. Dried at room temperature, the probe DNA modified electrode (S1/NCDs@CuO/ZnO/ITO) based on the covalent-linking reaction between S1 and NCDs was successfully fabricated.

Hybridization reaction of the modified electrode

The S1/NCDs@CuO/ZnO/ITO was put into a 200-μL different concentration of S2 and incubated at 42 °C for 40 min. Then, it was washed with TE buffer solution to remove the un-hybridized S2. The hybridized electrode was termed S2-S1/NCDs@CuO/ZnO/ITO. The hybridization of S1/NCDs@CuO/ZnO/ITO with S3, S4, and S5 DNA sequences was performed with same experimental steps.

Results and discussion

Characterization of prepared materials

The morphology and microstructure of the synthesized products were investigated by FESEM and TEM. As well seen in Fig. 1A and insert of Fig. 1A, the shape of Cu-TPA was similarly microsphere structured with the diameter range of 0.5 ~ 11 μm, which also indicated that the good crystallinity of the Cu-TPA was obtained. From the enlarged SEM image (Fig. 1B), a large number of micro-pores could be observed on Cu-TPA. Compared to the Cu-TPA precursor, CuO/ZnO composites had a much coarser surface with a distinct macropore in size of about 0.3 ~ 1.7 μm (Fig. 1C). In Fig. 1D, the ZnO particles were welded with the CuO microsphere to form the composite of CuO/ZnO. Figure 1E shows that the ZIF-8 had a typical rhombic dodecahedron structure with a smooth surface, and the average particle size was about 250 ~ 350 nm. In addition, the SEM image of Cu-TPA/ZIF-8 is shown in Fig. S2. The SEM results demonstrated that the CuO/ZnO composite still maintained the basic morphologies of their precursor templates of Cu-TPA or ZIF-8.

The microstructure characteristics of Cu-TPA and CuO/ZnO composite were further investigated in the TEM analysis. As seen in the insert of Fig. 1E, ZnO particles had a well-retained rhombus shape with a hollow structure. Compared to the pure Cu-TPA (insert of Fig. 1B), CuO microsphere displayed a thinner crystalline structure with a greater roughness of the microsphere edge (Fig. 1F and insert), which may be caused by the hyperthermia pyrolysis process. Meanwhile, distributed ZnO particles with a similar rhombic shape were also found in CuO/ZnO composite. The TEM result was in agreement with the SEM investigation of CuO/ZnO. Elemental mapping images (Fig. S3C) manifested the homogeneous distribution of Cu, Zn, O, and C elements in the hetero-structured composite of CuO/ZnO.

Figure S3A shows the TEM measurements of NCD nanoparticles. It was found that the spherical-like shapes of NCDs were continuously distributed, and an average diameter of NCDs was determined to be 18 ~ 23 nm. From the HRTEM image (Fig. S3B and insert), the typical lattice spacing of 0.34 nm corresponded to a graphitic structure of the NCDs [42], which also proved that the NCDs had been successfully synthesized.

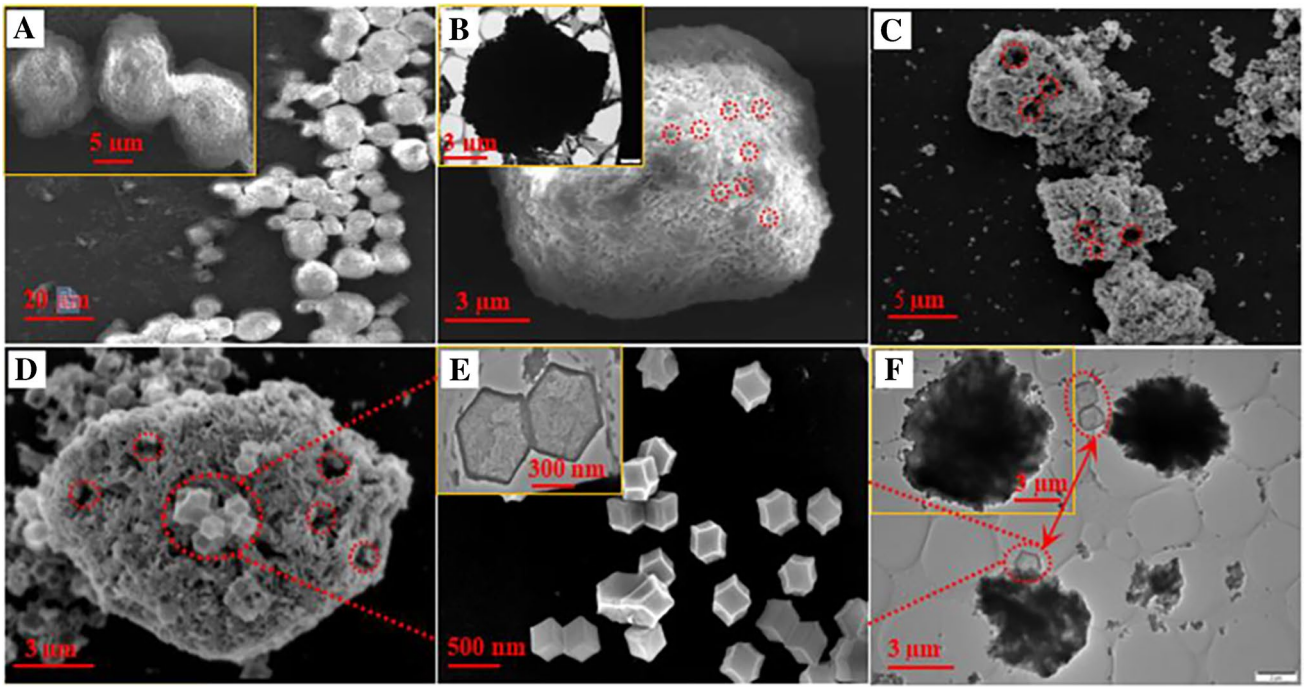

Fig. 1 Low magnification and high magnification SEM images of (**A** and inset of **A**, **B**) Cu-TPA, (**C**, **D**) CuO/ZnO, and (**E**) ZIF-8; TEM images of (inset of **B**) Cu-TPA, (inset of E) ZIF-8, and (**F**) CuO/ZnO

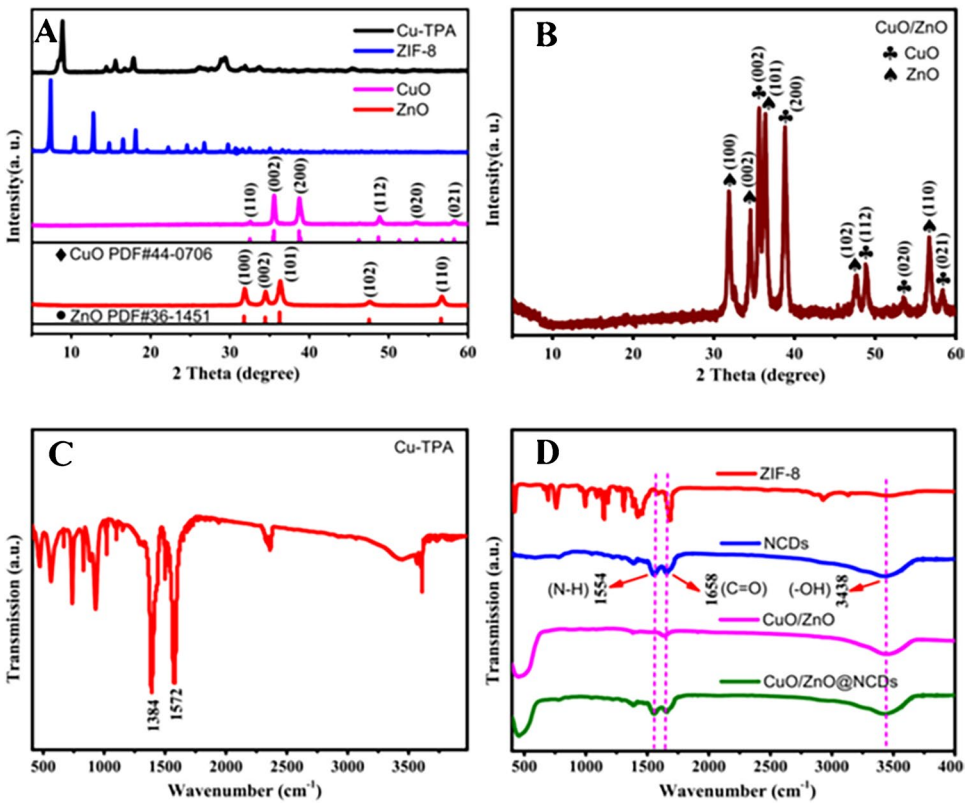

Fig. 2 XRD patterns of (**A**) Cu-TPA, ZIF-8, CuO, ZnO and (**B**) CuO/ZnO, FT-IR spectra of (**C**) Cu-TPA and (**D**) ZIF-8, NCDs, CuO/ZnO, NCDs@CuO/ZnO

The phase composite and crystal structure of the synthesized products were examined by XRD pattern. As seen in Fig. 2A, the characteristic diffraction peaks of Cu-TPA and ZIF-8 were in good agreement with the literature reported [43, 44], respectively, indicating that the Cu-TPA and ZIF-8 had been prepared successfully with high purity. The diffraction peaks at 32.5°, 35.5°, 38.8°, 48.8°, 53.5°, and 58.33° observed in XRD pattern were indexed to the characteristic (110), (002), (200), (112), (020), and (021) planes of CuO (PDF#04–0706). The peaks at 31.8°, 34.7°, 36.7°, 47.7°, and 56.3° could be indexed to (100), (002), (101), (102), and (110) planes of ZnO (PDF#36–1451). Figure 2B shows the strong and sharp diffraction peaks of CuO and ZnO, testifying that the CuO/ZnO composite was successfully synthesized. The typical XRD pattern of NCDs with the $2\theta = 24.8°$ is also shown in Fig. S4A. Figure S4B shows the thermogravimetric (TG) patterns of Cu-TPA and Cu-TPA/ZIF-8, in which both products could be stable up to approximately 320 °C. It was noteworthy that Cu-TPA/ZIF-8 had been decomposed at the temperature of 400 °C.

The FT-IR pattern of the synthesized products was determined by FT-IR spectroscopy. As seen in Fig. 2C, the characteristic peak values of 1384 cm^{-1} and 1572 cm^{-1} of Cu-TPA coincided with the reported literature [41]. Figure 2D shows the FT-IR pattern of ZIF-8, NCDs, CuO/ZnO, and NCDs@CuO/ZnO. The characteristic peaks at 1554 cm^{-1}, 1658 cm^{-1}, and 3834 cm^{-1} were assigned to the N–H, C = O, and O–H bonds of NCDs [45], respectively, which are also preserved in NCDs@CuO/ZnO. In addition, the characteristic peak at about 500 cm^{-1} was ascribed to the specific vibration of the Cu–O bond in CuO/ZnO and NCDs@CuO/ZnO. The Raman spectrum of CuO/ZnO is shown in Fig. S4C, in which two typical peaks at 1365 cm^{-1} and 1568 cm^{-1} were ascribed to the D-band and G-band, respectively.

The surface composition and chemical bonding state of the synthesized products were also investigated using XPS measurement. Figure 3A shows the XPS survey spectra of CuO, NCDs, and CuO/ZnO with their composing elements of Cu, Zn, N, O, and C, respectively. Figure 3B shows the high-resolution Cu 2p core-level spectrum of CuO/ZnO at about 933.6 and 953.6 eV which correspond to the Cu $2p_{3/2}$ and Cu $2p_{1/2}$ peaks, respectively, indicating that the oxidation state of Cu in CuO/ZnO was + 2 [46]. Meanwhile, two shakeup satellite peaks at approximately 941.3 and 962.1 eV also revealed the copper oxidation state of + 2. The high-resolution Cu 2p, O1s, and C 1 s spectra of CuO are shown in Fig. S5A ~ C. Figure 3C displays that the peaks at 1022.0 eV and 1045.1 eV were attributed to Zn $3d_{3/2}$ and Zn $3d_{1/2}$ of Zn^{2+} in CuO/ZnO [47]. Figure 3D shows the O1s spectra with two peaks at about 529.7 eV and 530.6 eV, which was attributed to the existence of O^{2-} in Cu–O and Zn–O bonding linker [48]. Meanwhile, the high-resolution N1s spectrum of NCDs was observed at about 962.1 eV, and the peaks that appeared at 284.7 eV and 287.7 eV (Fig. S5D ~ F) may

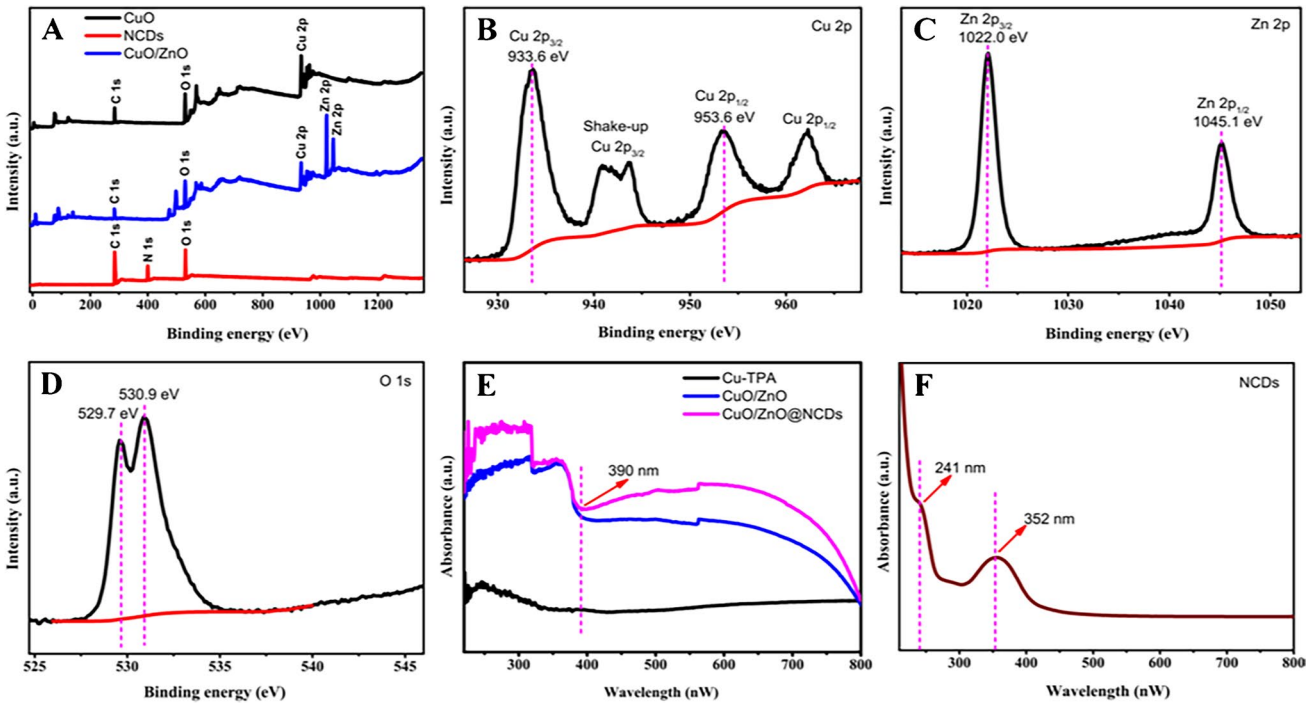

Fig. 3 XPS spectra of (**A**) CuO, NCDs, CuO/ZnO, High-resolution XPS spectra of (**B**) Cu 2p, (**C**) Zn 2p, (**D**) O 1 s of CuO/ZnO; UV–vis spectra of (**E**) Cu-TPA, CuO/ZnO, NCDs@CuO/ZnO, and (**F**) NCDs

be attributed to the C–C/C = C and C–OH/C–O–C bonds in NCDs [49], respectively. All above XPS results verified that the desired materials were successfully synthesized.

The UV–vis absorbance performance of prepared materials was investigated by diffuse reflectance spectroscopy (DRS). As observed in Fig. 3E, the pure Cu-TPA only had the photo-absorption property in the UV-light region, while the NCDs showed two absorption peaks of UV-light at about 241 and 352 nm (Fig. 3F), which was ascribed to the π–π* transition of C = C bond and the n–π* transition of C = O bond [42], respectively. Compared with pure Cu-TPA and NCDs, CuO/ZnO and NCDs@CuO/ZnO not only had remarkable absorption in the UV-light region but also showed obvious absorption properties in the visible-light region of $\lambda > 390$ nm. The result could be attributed to the heterogeneous interface composites formed among the CuO, ZnO, and NCDs. Furthermore, NCDs@CuO/ZnO displayed a better harvesting ability for visible-light than CuO/ZnO, demonstrating that the NCD nanoparticles could effectively sensitize the composite of CuO/ZnO.

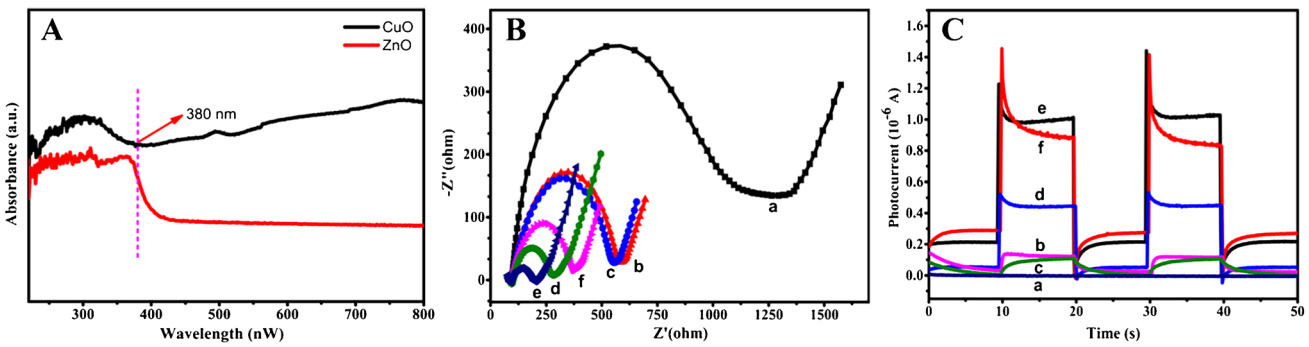

Fig. 4 (**A**) UV–vis spectrum of CuO and ZnO; (**B**) EIS and (**C**) PEC response of Cu-TPA/ZIF-8/ITO (**a**), CuO/ZIF-8/ITO (**b**), CuO/ITO (**c**), CuO/ZnO/ITO (**d**), NCDs@CuO/ZnO/ITO (**e**), S1/NCDs@CuO/ZnO/ITO (**f**); EIS and PEC experiments were conducted in 5 mM $[Fe(CN)_6]^{3-/4-}$ containing 0.1 M KCl and in 0.1 M PBS (pH 7.4), respectively

PEC mechanism

The UV–vis DRS of CuO and ZnO were also surveyed (Fig. 4A). It was found that the light absorption ability of ZnO declined at the wavelength of 380 nm, while the absorption intensity of CuO gradually enhanced in a range from 380 to 800 nm. This phenomenon could be explained by the thin-wall structure of the CuO microsphere which led to generating multiple scattering/reflection effects. In addition, based on the $(ahv)^2$ versus (hv) plots with the following empirical equation [9]: $ahv = A\ (hv - Eg)^{1/2}$, where hv, a, and A belong to the photon energy, a constant, and absorption coefficient, respectively. The Eg values of CuO, ZnO, and NCDs were estimated to be about 1.78, 3.20, and 2.98 eV (Fig. S6A ~ C), respectively. Meanwhile, using the valence band (VB)–XPS spectra, the VB potentials of CuO and NCDs were calculated at about 0.68 and 2.16 eV (Fig. S6D and E). The CB potentials could be obtained according to the empirical formula of $E_{CB} = E_{VB} - Eg$ (E_{CB} and E_{VB} were the CB and VB edge potentials, respectively). Hence, the corresponding CB potentials of CuO and NCDs were − 1.10 and − 0.82 eV. Additionally, the E_{VB} value of ZnO was 2.16 eV based on its CB positions value of − 0.5 eV [50, 51]. These results revealed that the narrower Eg value of CuO was compared with the ZnO and NCDs, and the CB and VB potentials of CuO were higher than that of NCDs and ZnO. Therefore, the composite of CuO, ZnO, and NCDs was assembled onto the ITO electrode to form tri-heterostructures. Under visible-light excitation, the photo-excited electrons in the CB of CuO were transferred to the CB of NCDs and ZnO orderly, while the holes in the VB of ZnO were transferred to the VB of NCDs and CuO subsequently, resulting in an enhanced photocurrent response. The significantly increased property of photo-to-electron was mostly attributed to the thin-shell structure of CuO microsphere with hollow ZnO particles which could extend the visible-light capture. Besides, the interlaced band structures of NCDs@CuO/ZnO formed tri-heterojunction could effectively separate the photo-generated e^{-1}/h^{+}. The last but not least, the high electro-catalysis of NCDs further facilitated the electron transfer. When the special DNA sequences (S1, S2) were introduced, the photocurrent values had decreased visibly due to their inferior conductivity. The detection mechanism of the DNA biosensor is shown in Scheme 1B.

Electrochemical and PEC behavior of the modified electrodes

Electrochemical impedance spectroscopy (EIS) was an effective tool that reflected the interface properties of modified electrodes [52]. In EIS, the electron-transfer resistance (R_{et}) value can be estimated by measuring a semicircle diameter at higher frequencies equals. As shown in Fig. 4B, the Cu-TPA/ZIF-8/ITO electrode (curve a) obtains the greatest R_{et} value of 1180 Ω, which indicated a very poor electron transferring ability on the electrode surface. The modified electrodes of CuO/ZIF-8/ITO (curve b) and CuO/ITO (curve c) possessed the approximate R_{et} values of 473 Ω and 486 Ω, respectively, while the R_{et} value on CuO/ZnO/ITO (curve d) decreased substantially (190 Ω) that was ascribed to the synergistic effect of CuO/ZnO composite that could improve the electrochemical property on the electrode surface. NCDs@CuO/ZnO/ITO electrode (curve e) exhibited a smaller arc radius with the R_{et} value of 103 Ω, indicating that NCDs promoted the electron transfer rate of the redox probe of $[Fe(CN)_6]^{3-/4-}$ owing to the excellent electric conductivity. When the probe DNA (S1) was immobilized on NCDs@CuO/ZnO/ITO electrode, the R_{et} value significantly boosted (curve f, 292 Ω) due to negatively charged phosphate backbone with the steric hindrance effect of S1 which inhibited the electron transfer of $[Fe(CN)_6]^{3-/4-}$. The preparation process of the modified electrode was also investigated by CVs (Fig. S6F and Fig. S7A). All the EIS and CV results prove that the S1/NCDs@CuO/ZnO/ITO electrode was fabricated successfully.

To deeply study the photoelectric property of various modified electrodes, all photoelectric tests were recorded in 0.1 M PBS (pH 7.4) and the results are shown in Fig. 4C. It was obvious that the photocurrent response on Cu-TPA/ZIF-8/ITO (curve a) was almost zero. Compared with Cu-TPA/ZIF-8/ITO, the photocurrent values of CuO/ZIF-8/ITO and CuO/ITO (0.12 μA and 0.1 μA, curves b and c) were increasing obviously. This result was due to the porous thin structure of the CuO microsphere that had good charge penetration property. On the CuO/ZnO/ITO electrode (curve d), the photocurrent intensity increased to 0.45 μA, which was ascribed to the p-n type heterogeneous construction of CuO/ZnO composite that could accelerate the photo-generated electron/hole pair separation. Nevertheless, the photocurrent responses of NCDs@CuO/ZnO/ITO (curve e) had the biggest value (1.03 μA), which was 2.28-fold than that of CuO/ZnO/ITO and 10.3-fold than that of CuO/ITO, respectively, indicating that the more efficient sensitization effect with higher conductivity of NCDs could enlarge remarkably the photocurrent strength. Afterward, the photocurrent intensity of S1/NCDs@CuO/ZnO/ITO decreased slightly (curve f) due to the hindrance effect and low conductivity of S1. The PEC results confirmed that this sensing interface for DNA detection was proposed successfully.

The linear sweep voltammetry (LSV) tests of NCDs@CuO/ZnO, CuO/ZnO, CuO, and Cu-TPA/ZIF-8 were carried out in 0.1 M Na_2SO_4 at a potential range of 0.0 ~ 0.75 V vs. Ag/AgCl. As shown in Fig. 5A, the LSV curve of Cu-TPA/ZIF-8 exhibited no photocurrent effect under continuous visible-light irradiation because of the much great

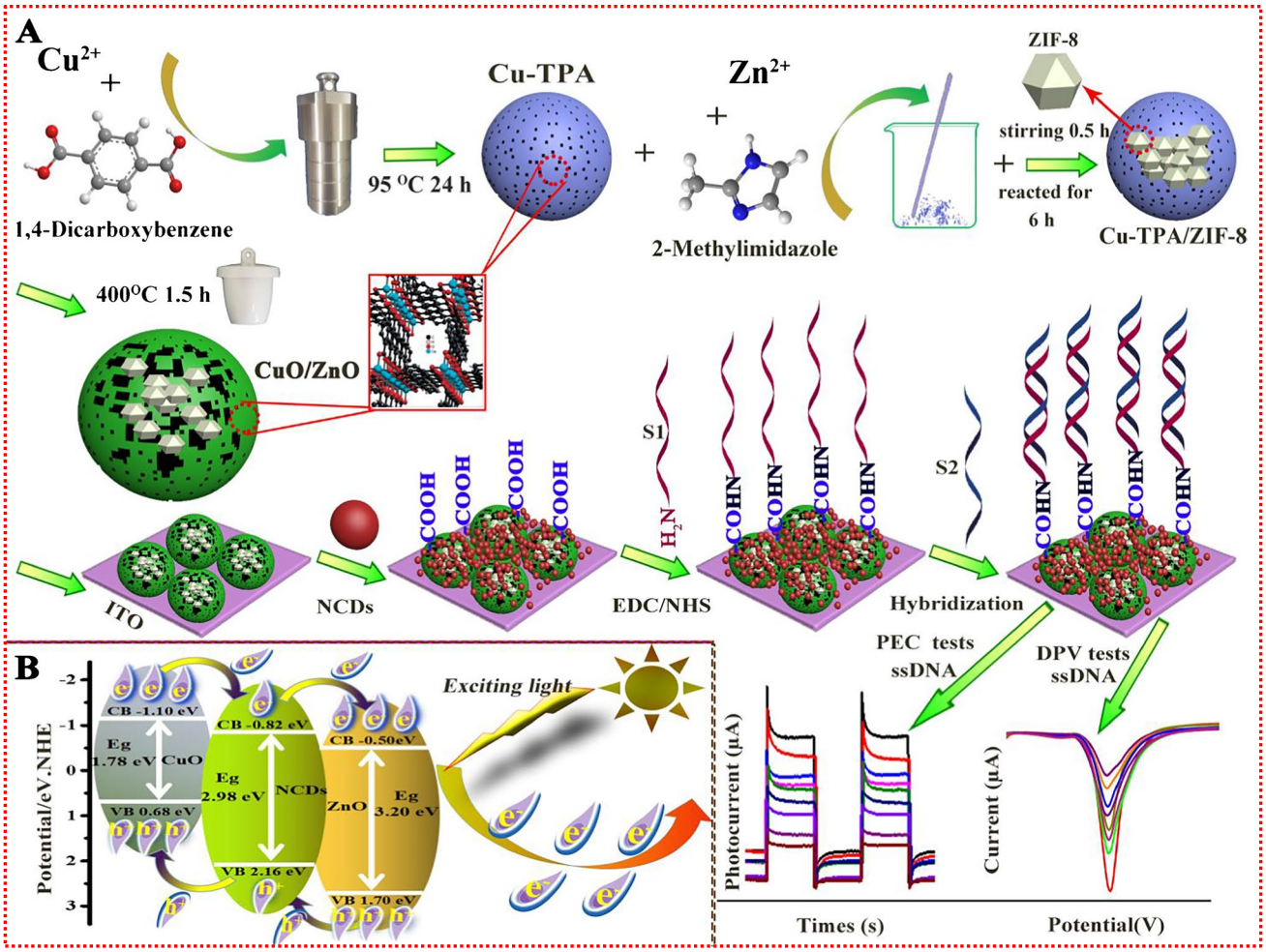

Scheme 1 (**A**) Schematic illustration of the synthesis process of CuO/ZnO and the construction processes of PEC and DPV biosensors for colitoxin DNA detection. (**B**) Photogenerated electron–hole transfer mechanism based on NCDs@CuO/ZnO

recombination rate of photo-generated e^{-1}/h^{+} pairs. However, the photocurrent response of LSV on CuO and CuO/ZnO showed an escalating trend, which demonstrated that the heterojunction composite of CuO/ZnO could facilitate photo-generated e^{-1}/h^{+} pair transfer and separate speedily. It was noted that the highest LSV response was obtained on NCDs@CuO/ZnO; this reason could be attributed to the excellent conductivity of NCDs which could further enhance the PEC property.

The open-circuit potential (OCP) patterns of NCDs@CuO/ZnO, CuO/ZnO, and CuO under dark and visible-light irradiation were recorded in 0.1 M PBS (pH 7.4) solution. As depicted in Fig. 5B, the feature peak of OCP on CuO verified that the presence of n-type CuO. In the dark, the proposed materials of CuO, CuO/ZnO, and NCDs@CuO/ZnO all displayed a downward surface band bending (region I) due to the potential of redox equilibration [53]. Under continuous illumination owing to the photo-generated electrons accumulating, the OCP response of the above materials increases quickly towards a positive Fermi level and reaches a steady state (region II). After the irradiation was switched off, the OCP intensity gradually decreased (region III), which may be ascribed to the recombination of photo-generated charge carriers [36]. In addition, the change values of OCP (ΔOCP) could manifest the charge separation efficiency of different modified materials; it was easily found that the ΔOCP values of CuO/ZnO and NCDs@CuO/ZnO both exhibited greater than the single-component material of CuO, demonstrating that p-n type heterogeneous composites got more photo-generated electrons and both accelerated charge carriers change efficiently. These OCP results also revealed that the NCD nanoparticles could achieve the photo-sensitive effect for CuO/ZnO.

PEC analysis properties of the prepared biosensor

Under optimized conditions, the developed DNA biosensor was applied to detect different concentrations of colitoxin

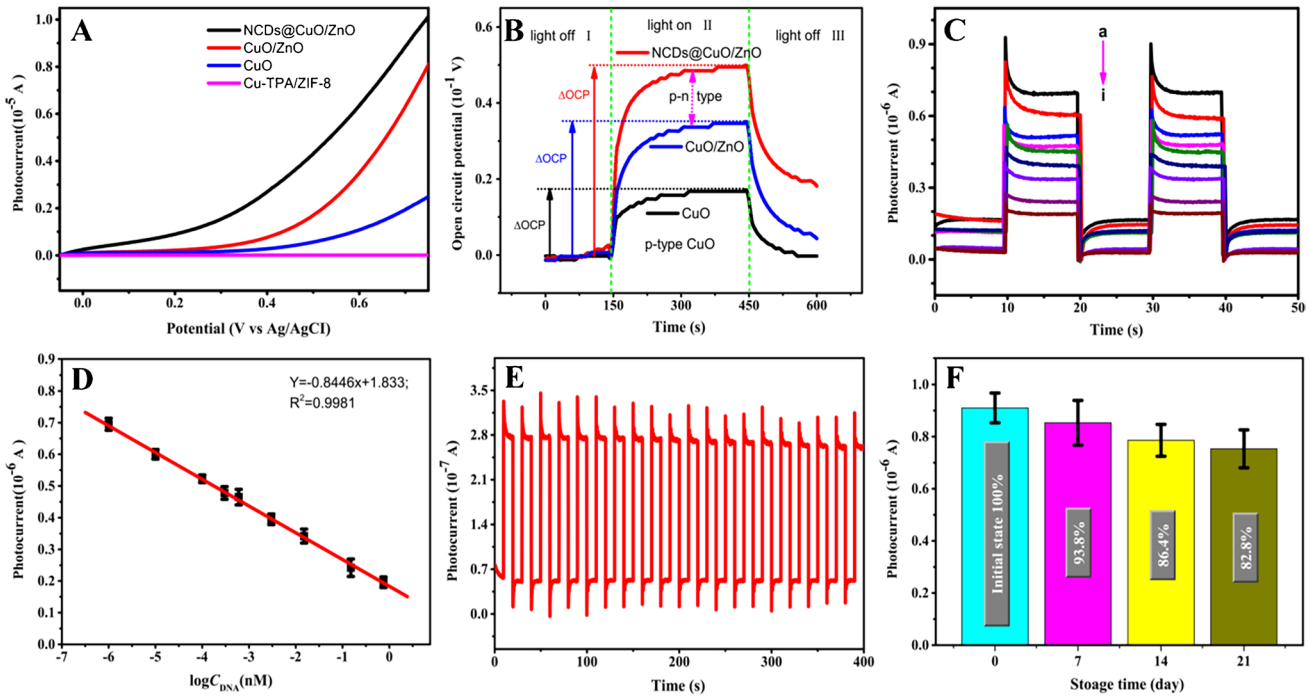

Fig. 5 (**A**) LSV patterns of NCDs@CuO/ZnO, CuO/ZnO, CuO, and Cu-TPA/ZIF-8 in 0.1 M Na_2SO_4 with a scan rate of 80 mV s^{-1}, (**B**) OCP curves of NCDs@CuO/ZnO, CuO/ZnO, CuO in 0.1 M PBS (pH 7.4); (**C**) PEC response and (**D**) the corresponding logarithmic curve of S1/NCDs@CuO/ZnO/ITO sensor for the detection of different concentrations of target DNA (S2). (a–i) 1.0×10^{-6}, 1.0×10^{-5}, 1.0×10^{-4}, 3.0×10^{-4}, 6.0×10^{-4}, 3.0×10^{-3}, 1.5×10^{-2}, 1.5×10^{-1}, 7.5×10^{-1} nM; (**E**) time-based photocurrent response of S2-S1/NCDs@CuO/ZnO/ITO electrodes with light on and off cycles; (**F**) the photocurrent responses of as-prepared biosensor after different storage time (day) in PBS (0.1 M, pH 7.4)

DNA (S2). Figure 5C shows the photocurrent response gradually decreases with increasing concentrations of S2, suggesting that more and more double-helix structure of DNA had been formed on the modified electrode surface, and the photocurrent change values (ΔI) were commendably proportional to the logarithm of the target DNA concentration (log C_{S2}) from 1.0×10^{-6} to 7.5×10^{-1} nM (Fig. 5D). The linear equation was ΔI (μA) = -0.8446 log C_{DNA} (nM) + 1.833 ($R^2 = 0.9981$) and with a low LOD value of 1.81×10^{-7} nM based on 3 signal-to-noise ratio (S/N = 3). To further probe whether this PEC biosensor had the best analytical performance for target DNA, S1/NCDs@CuO/ZnO/ITO hybridization response with different concentrations of S2 was also investigated by the electrochemical method of DPV. Figure S9B and C show the change values of DPV increased accordingly with the increase of S2 concentration (C_{S2}) in the range from 1.0×10^{-5} to 2.5×10^{-2} nM with a LOD value of 2.43×10^{-6} nM (S/N = 3). Through comparison of this result and others reported in the literature (shown in Table S1), it could be found that the prepared PEC biosensor exhibited a wider linear range. This superior analytic ability may be attributed to that NCDs@CuO/ZnO composites had the mainly photoelectric activity compared with its electrochemical property, and as well the synergetic amplifying effect of multiple heterogeneous architectures with a contact interface.

Stability, selectivity, and reproducibility of PEC biosensor

Figure 5E shows the stability of the prepared PEC biosensor; it was found that no significant photocurrent signals change on S1/NCDs@CuO/ZnO/ITO modified electrodes after the biosensors hybridization with 8.0×10^{-2} nM colitoxin DNA under irradiation cycles for 400 s and when on/off, which demonstrated that the developed PEC biosensor had superior long-term stability for target DNA analysis. When the fabricated PEC biosensor was stored for a week at 4 °C, the photocurrent was reduced to 93.8% compared with the original photocurrent intensity (100%). When the storage time exceeded 2 weeks, the photocurrent declined to 86.4% (Fig. 5F), suggesting that the modified electrode had the receivable stability.

Figure S7C shows the selectivity investigation of fabricated colitoxin DNA sensor hybridization with the complementary DNA sequence (S2), non-complementary DNA sequence (S5), and the mismatch DNA sequences: single-base mismatched DNA (S3) and three-base mismatched

DNA (S4). At the depiction of PEC results, S1/NCDs@CuO/ZnO/ITO electrode had the highest PEC responses. After the biosensor was hybridized with S2 (curve e), the PEC signals significantly decreased, indicating the efficient hybridization reaction occurrence on the electrode surface. When the biosensor was hybridized with S5 (curve b), the photocurrent change was negligible, suggesting that the non-specific absorption did not occur. When this biosensor was hybridized with S3 (curve d) and S4 (curve c), the decreased photocurrent signals were still higher than that obtained on the hybridized electrode with S2, displaying that the S3 and S4 DNA sequences only occurred as partial hybridization with the S1. The corresponding histogram of photocurrent values is shown in Fig. S9A, demonstrating that the developed photochemical biosensors possessed excellent selectivity.

The reproducibility of the biosensor was studied by comparing the PEC response current of three equilibrium results of S1/NCDs@CuO/ZnO/ITO electrode after hybridization with 5.0×10^{-2} nM target DNA. The obtained relative standard deviation (RSD) was corresponding to 6.3%, indicating that the fabricated biosensors had satisfactory reproducibility.

Conclusion

In this work, the MOF-derived hetero-structured composite of CuO/ZnO was synthesized, and the MOF-derived morphologies of CuO/ZnO particles possessed the advantage for harvesting UV–visible light. The porous flaw structure of CuO/ZnO was profitable for the electrolytic ion accessing. The obtained compact contact interface of CuO/ZnO could reduce the transport distance of the charge carriers. CuO/ZnO was coupled with NCDs to form the hierarchical band gap energies architecture that could further accelerate charge carrier separation and migration. This tri-heterogeneous composite of NCDs@CuO/ZnO modified ITO electrode resulted in a remarkable PEC signal response. The PEC analysis results of proposed biosensor displayed a better sensing performance than the DPV characterization method. In general, this work broadened the practical application of the MOF-derivative, and the proposed method provided a promising strategy for the inexpensive, accurate, and convenient detection of DNA in the bio-molecular diagnostic areas.

In this paper, the tri-heterostructured NCDs@CuO/ZnO system and its PEC mechanism were initially explored. Further work will be focused on the construction of novel heterojunctions and to improve the practical application ability in other fields.

Supplementary Information The online version contains supplementary material available at https://doi.org/10.1007/s00604-022-05280-y.

Funding This work was financially supported by the Guangdong Basic and Applied Basic Research Foundation (No. 2019A1515010618), the Guangdong Special Funds for the Science & Technology Project (No. 2019ST029 & No. 2019ST089), 2020 Li Ka Shing Foundation Cross-Disciplinary Research Grant (Project Number 2020LKSFG06C), and Shantou Polytechnic Supported Project (No. 2019SZK2019Y01).

Declarations

Conflict of interest The authors declare no competing interests.

References

1. Chang J, Lv W, Li Q, Li H, Li F (2020) One-step synthesis of methylene blue-encapsulated ZIF for dual-signal fluorescent and homogeneous electrochemical biosensing. Anal Chem 92:8959–8964. https://doi.org/10.1021/acs.analchem.0c00952
2. Chang J, Lv W, Wu J, Li H, Li F (2021) Simultaneous photoelectrochemical detection of dual microRNAs by capturing CdS quantum dots and methylene blue based on target-initiated strand displaced amplification. Chin Chem Lett 32:775–778. https://doi.org/10.1016/j.cclet.2020.05.041
3. Qian Z, Bai H, Wang G, Xu J, Chen H (2010) A photoelectrochemical sensor based on CdS-polyamidoamine nano-composite film for cell capture and detection. Biosens Bioelectron 25:2045–2050. https://doi.org/10.1016/j.bios.2010.01.036
4. Long D, Li M, Wang H, Chai Y, Li Z, Yuan R (2020) Ultrasensitive photoelectrochemical assay for DNA detection based on a novel SnS_2/Co_3O_4 sensitized structure. Anal Chem 92:14769–14774. https://doi.org/10.1021/acs.analchem.0c03497
5. Chen F, Han D, Chen H (2020) Liposome-assisted enzymatic modulation of plasmonic photoelectrochemistry for immunoassay. Anal Chem 92:8450–8458. https://doi.org/10.1021/acs.analchem.0c01162
6. Guo J, Liu D, Yang Z, Weng W, Chan E, Zeng Z, Wong K, Lin P, Chen S (2020) A photoelectrochemical biosensor for rapid and ultrasensitive norovirus detection. Bioelectrochemistry 136:107591. https://doi.org/10.1016/j.bioelechem.2020.107591
7. Yu X, Wang Y, Chen X, Wu K, Chen D, Ma M, Huang Z, Wu W, Li C (2015) White-light-exciting, layer-by-layer-assembled ZnCdHgSe quantum dots/polymerized ionic liquid hybrid film for highly sensitive photoelectrochemical immunosensing of neuron specific enolase. Anal Chem 87:4237–4244. https://doi.org/10.1021/ac504456w
8. Li F, Zhou Y, Wang S, Yin H, Chen Y, Luo H, Ai S (2020) One step preparation of CN-WS_2 nanocomposite with enhanced photoactivity and its application for photoelectrochemical detection of 5-formylcytosine in the genomic DNA of maize seedling. Biosens Bioelectron 151:111973. https://doi.org/10.1016/j.bios.2019.111973
9. Zheng D, Chen M, Peng J, Jiayang Chen J, Chen T, Chen Y, Huang L, Gao W (2021) An enhanced photoelectrochemical biosensor for colitoxin DNA based on HKUST-1/TiO_2 and derived HKUST-CuO/TiO_2 heterogeneous composites. Microchim Acta 188(10):328–338. https://doi.org/10.1007/s00604-021-04999-4
10. Wu F, Yu Y, Yang H, German L, Li Z, Chen J, Yang W, Huang L, Shi W, Wang L, Wang X (2017) Simultaneous enhancement of charge separation and hole transportation in a TiO_2–$SrTiO_3$ core–shell nanowire photoelectrochemical system. Adv Mater 29:1701432. https://doi.org/10.1002/adma.201701432
11. Li C, He J, Xiao Y, Li Y, Delaunay J-J (2020) Earth-abundant Cu-based metal oxide photocathodes for photoelectrochemical water

splitting, Energy Environ. Sci 13:3269–3306. https://doi.org/10.1039/D0EE02397C
12. Yang C, Wu Q, Jiang Z, Wang X, Huang C, Li Y (2021) Cu vacancies enhanced photoelectrochemical activity of metal-organic gel-derived CuO for the detection of L-cysteine. Talanta 228:122261–122268. https://doi.org/10.1016/j.talanta.2021.122261
13. Shao M, Ning F, Wei M, Evans D, Duan X (2014) Hierarchical nanowire arrays based on ZnO core-layered double hydroxide shell for largely enhanced photoelectrochemical water splitting. Adv Funct Mater 24:580–586. https://doi.org/10.1002/adfm.201301889
14. Bondarenko E, Streltsov E, Malashchonak M, Mazanik A, Kulak A, Skorb E (2017) Giant incident photon-to-current conversion with photoconductivity gain on nanostructured bismuth oxysulfide photoelectrodes under visible-light illumination. Adv Mater 29:1702387. https://doi.org/10.1002/adma.201770287
15. Qiu B, Zhu Q, Du M, Fan L, Xing M, Zhang J (2017) Efficient solar light harvesting CdS/Co_9S_8 hollow cubes for Z-Scheme photocatalytic water splitting. Angew Chem Int Ed 56:2684–2688. https://doi.org/10.1002/anie.201612551
16. Septina W, Prabhakar R, Wick R, Moehl T, Tilley SD (2017) Stabilized solar hydrogen production with CuO/CdS heterojunction thin film photocathodes. Chem Mater 29:1735–1743. https://doi.org/10.1021/acs.chemmater.6b05248
17. Trang T, Phan T, Nam N, Thu V (2020) In situ charge transfer at the Ag@ZnO photoelectrochemical interface toward the high photocatalytic performance of H_2 evolution and RhB degradation. ACS Appl Mater Interfaces 12:12195–12206. https://doi.org/10.1021/acsami.9b15578
18. Petrella A, Cozzoli PD, Curri ML, Striccoli M, Cosma P, Agostiano A (2004) Photoelectrochemical study on photosynthetic pigments-sensitized nanocrystalline ZnO films. Bioelectrochem 63:99–102. https://doi.org/10.1016/j.bioelechem.2003.09.016
19. Low JX, Yu JG, Jaroniec M, Wageh S, Al-Ghamdi AA (2017) Heterojunction photocatalysts. Adv Mater 29:1601694. https://doi.org/10.1002/adma.201601694
20. Bhat S, Pawar S, Potphode D, Moon C, Suh J, Kim C, Choi S, Patil D, Kim J, Shin J, Jang H (2019) Substantially enhanced photoelectrochemical performance of TiO_2 nanorods/CdS nanocrystals heterojunction photoanode decorated with MoS_2 nanosheets. Appl Catal B Environ 259:118102. https://doi.org/10.1016/j.apcatb.2019.118102
21. Kment S, Riboni F, Pausova S, Wang L, Wang L, Han H, Hubicka Z, Krysa J, Schmuki P, Zboril R (2017) Photoanodes based on TiO_2 and a-Fe_2O_3 for solar water splitting-superior role of 1D nanoarchitectures and of combined heterostructures. Chem Soc Rev 46:3716–3769. https://doi.org/10.1039/C6CS00015K
22. Peng H, Raya J, Richard F, Baaziz W, Ersen O, Ciesielski A, Samori P (2020) Synthesis of robust MOFs@COFs porous hybrid materials via an aza-diels-alder reaction: towards high-performance supercapacitor materials. Angew Chem Int Ed 59:19602–19609. https://doi.org/10.1002/ange.202008408
23. Dhakshinamoorthy A, Li Z, Garcia H (2018) Catalysis and photocatalysis by metal organic frameworks. Chem Soc Rev 47:8134–8172. https://doi.org/10.1039/C8CS00256H
24. Ding Y, Zhang X, Peng J, Zheng D, Zhang X, Song Y, Chen Y, Gao W (2020) Ultra-sensitive electrochemiluminescence platform based on magnetic metal-organic framework for the highly efficient enrichment. Sens Actuators B Chem 324:128700. https://doi.org/10.1016/j.snb.2020.128700
25. Huang G, Li Q, Yin D, Wang L (2017) Hierarchical porous Te@$ZnCo_2O_4$ nanofibers derived from Te@metal-organic frameworks for superior lithium storage capability. Adv Funct Mater 27:1604941. https://doi.org/10.1002/adfm.201604941
26. Guo Y, Tang J, Qian H, Wang Z, Yamauchi Y (2017) One-pot synthesis of zeolitic imidazolate framework 67-derived hollow Co_3S_4@MoS_2 heterostructures as efficient bifunctional catalysts. Chem Mater 29:5566–5573. https://doi.org/10.1021/acs.chemmater.7b00867
27. Tang R, Zhou S, Li H, Chen R, Zhang L, Yin L (2020) Halogen bonding induced aqueously stable CsPbBr 3@MOFs-derived C_o3_O4/N-doped-C heterostructure for high-performance photoelectrochemical water oxidation. Appl Catal B Environ 265:118583. https://doi.org/10.1016/j.apcatb.2019.118583
28. Zhao X, Feng J, Liu J, Lu J, Shi W, Yang G, Wang G, Feng P, Cheng P (2018) Metal-organic framework-derived ZnO/ZnS heteronanostructures for efficient visible-light-driven photocatalytic hydrogen production. Adv Sci 5:1700590. https://doi.org/10.1002/advs.201700590
29. Wang Q, Gao F, Xu B, Cai F, Zhan F, Gao F, Wang Q (2017) ZIF-67 derived amorphous $CoNi_2S_4$ nanocages with nanosheet arrays on the shell for a high-performance asymmetric supercapacitor. Chem Eng J 327:387–396. https://doi.org/10.1016/j.cej.2017.06.124
30. Hu X, Li C, Lou X, Yang Q, Hu B (2017) Hierarchical CuO octahedra inherited from copper metal-organic frameworks: high-rate and high-capacity lithium-ion storage materials stimulated by pseudocapacitance. J Mater Chem A 5:12828–12837. https://doi.org/10.1039/C7TA02953E
31. Zhang Y, Qiu L, Yuan Y, Zhu Y, Jiang X, Xiao J (2014) Magnetic Fe_3O_4@C/Cu and Fe_3O_4@CuO core-shell composites constructed from MOF-based materials and their photocatalytic properties under visible light. Appl Catal B Environ 144:863–869. https://doi.org/10.1016/j.apcatb.2013.08.019
32. Zhang X, Peng J, Ding Y, Zheng D, Lin Y, Chen Y, Gao W (2020) Rationally designed hierarchical hollow ZnCdS@MoS_2 heterostructured cages with efficient separation of photogenerated carriers for photoelectrochemical aptasensing of lincomycin. Sens Actuators B Chem 306:127552. https://doi.org/10.1016/j.snb.2019.127552
33. Xu R, Gu Y, Ploehn H, Gearheart L, Raker K, Scrivens W (2004) Electrophoretic analysis and purification of fluorescent single-walled carbon nanotube fragments. J Am Chem Soc 126:12736–12737. https://doi.org/10.1021/ja040082h
34. Lv W, Wang X, Wu J, Li H, Li F (2019) pH and H_2O_2 dual-responsive carbon dots for biocatalytic transformation monitoring. Chin Chem Lett 30:1635–1638. https://doi.org/10.1016/j.cclet.2019.06.029
35. Vazquez-Gonzalez M, Liao W, Cazelles R, Wang S, Yu X, Gutkin V, Willner I (2017) Mimicking horseradish peroxidase functions using Cu^{2+}-modified carbon nitride nanoparticles or Cu^{2+}-modified carbon dots as heterogeneous Catalysts. ACS Nano 11:3247–3253. https://doi.org/10.1021/acsnano.7b00352
36. Liu C, Lu D, You X, Shi G, Deng J, Zhou T (2020) Carbon dots sensitized lanthanide infinite coordination polymer nanoparticles: towards ratiometric fluorescent sensing of cerebrospinal Abeta monomer as a biomarker for Alzheimer's disease. Anal Chim Acta 1105:147–154. https://doi.org/10.1016/j.aca.2020.01.021
37. Nekoueian K, Amiri M, Sillanpää M, Marken F, Boukherroub R, Szunerits S (2019) Carbon-based quantum particles: an electroanalytical and biomedical perspective. Chem Soc Rev 48:4281–4316. https://doi.org/10.1039/C8CS00445E
38. Zhang G, Ji Q, Wu Z, Wang G, Liu H, Qu J, Li J (2018) Facile "spot-heating" synthesis of carbon dots/carbon nitride for solar hydrogen evolution synchronously with contaminant decomposition. Adv Funct Mater 28:1706462. https://doi.org/10.1002/adfm.201706462
39. Shi R, Li Z, Yu H, Shang L, Zhou C, Waterhouse G, Wu L, Zhang T (2017) Effect of nitrogen doping level on the performance of N-doped carbon quantum dot/TiO_2 composites for photocatalytic hydrogen evolution. Chemsuschem 10:4650–4656. https://doi.org/10.1002/cssc.201700943

40. Cheng W, Zheng Z, Yang J, Chen M, Yao Q, Chen Y, Gao W (2019) The visible light-driven and self-powered photoelectrochemical biosensor for organophosphate pesticides detection based on nitrogen doped carbon quantum dots for the signal amplification. Electrochim Acta 296:627–636. https://doi.org/10.1016/j.electacta.2018.11.086
41. Wang X, Wang Q, Wang Q, Gao F, Gao F, Yang Y, Guo H (2014) Highly dispersible and stable copper terephthalate metal-organic framework-graphene oxide nanocomposite for an electrochemical sensing application. ACS Appl Mater Interfaces 6:11573–11580. https://doi.org/10.1021/am5019918
42. Li Z, Yu H, Bian T, Zhao Y, Zhou C, Shang L, Liu Y, Wu LZ, Tung CH, Zhang T (2015) Highly luminescent nitrogen-doped carbon quantum dots as effective fluorescent probes for mercuric and iodide ions. J Mater Chem C 3:1922–1928. https://doi.org/10.1039/C4TC02756F
43. Carson CG, Hardcastle K, Schwartz J, Liu X, Hoffmann C, Gerhardt RA, Tannenbaum R (2009) Synthesis and structure characterization of copper terephthalate metal-organic frameworks. Eur J Inorg Chem 2009:2338–2343. https://doi.org/10.1002/ejic.200801224
44. Dong S, Li C, Ge X, Li Z, Miao X, Yin L (2017) ZnS-Sb_2S_3@C core-double shell polyhedron structure derived from metal-organic framework as anodes for high performance sodium ion batteries. ACS Nano 11:6474–6482. https://doi.org/10.1021/acsnano.7b03321
45. Huang Q, Lin X, Zhu J, Tong Q (2017) Pd-Au@carbon dots nanocomposite: Facile synthesis and application as an ultrasensitive electrochemical biosensor for determination of colitoxin DNA in human serum. Biosens Bioelectron 94:507–512. https://doi.org/10.1016/j.bios.2017.03.048
46. Cots A, Bonete P, Gomez R (2018) Improving the stability and efficiency of CuO photocathodes for solar hydrogen production through modification with Iron. ACS Appl Mater Interfaces 10:26348–26356. https://doi.org/10.1021/acsami.8b09892
47. Jeong K, Deshmukh PR, Park J, Sohn Y, Shin WG (2018) ZnO-TiO_2 core–shell nanowires: a sustainable photoanode for enhanced photoelectrochemical water splitting, ACS Sustainable Chem. Eng 6:6518–6526. https://doi.org/10.1021/acssuschemeng.8b00324
48. Kwiatkowski M, Bezverkhyy I, Skompska M (2015) ZnO nanorods covered with TiO_2 layer: simple sol-gel preparation, optical, photocatalytic and photoelectrochemical properties. J Mater Chem A 3:12748–12760. https://doi.org/10.1039/C5TA01087J
49. Han H, Karlicky F, Pitchaimuthu S, Shin S, Chen A (2019) Highly ordered N-doped carbon dots photosensitizer on Metal-Organic Framework-decorated ZnO nanotubes for improved photoelectrochemical water splitting. Small 15:1902771. https://doi.org/10.1002/smll.201902771
50. Jiang C, Moniz S, Wang A, Zhang T, Tang J (2017) Photoelectrochemical devices for solar water splitting-materials and challenges. Chem Soc Rev 46:4645–4660. https://doi.org/10.1039/c6cs00306k
51. Zhang X, Zhang R, Yang A, Qin Wang Q, Kong R, Qu F (2017) Aptamer based photoelectrochemical determination of tetracycline using a spindle-like ZnO-CdS@Au nanocomposite. Mikrochim Acta 184(11):4367–4374. https://doi.org/10.1007/s00604-017-2477-8
52. Zhuge W, Li X, Feng S, S, (2020) Visible-light photoelectrochemical sensor for glutathione based on $CoFe_2O_4$-nanosphere-sensitized copper tetraaminophthalocyanine–graphene oxide. Microchem J 155:104726–104732. https://doi.org/10.1016/j.microc.2020.104726
53. Kamimura J, Bogdanoff P, Ramsteiner M, Corfdir P, Feix F, Geelhaar L, Riechert H (2017) P-type doping of GaN nanowires characterized by photoelectrochemical measurements. Nano Lett 17:1529–1537. https://doi.org/10.1021/acs.nanolett.6b04560